

## UC Irvine

### UC Irvine Previously Published Works

**Title**

Manganese–Hydroxido Complexes Supported by a Urea/Phosphinic Amide Tripodal Ligand

**Permalink**

<https://escholarship.org/uc/item/5fq3p1dd>

**Journal**

Inorganic Chemistry, 57(21)

**ISSN**

0020-1669

**Authors**

Oswald, Victoria F  
Weitz, Andrew C  
Biswas, Saborni  
[et al.](#)

**Publication Date**

2018-11-05

**DOI**

10.1021/acs.inorgchem.8b01886

Peer reviewed



Published in final edited form as:

*Inorg Chem.* 2018 November 05; 57(21): 13341–13350. doi:10.1021/acs.inorgchem.8b01886.

## Manganese-Hydroxido Complexes Supported by a Urea/ Phosphinic Amide Tripodal Ligand

Victoria F. Oswald<sup>†</sup>, Andrew C. Weitz<sup>‡</sup>, Saborni Biswas<sup>‡</sup>, Joseph W. Ziller<sup>†</sup>, Michael P. Hendrich<sup>‡</sup>, and A. S. Borovik<sup>\*†</sup>

<sup>†</sup>Department of Chemistry, University of California-Irvine, 1102 Natural Sciences II, Irvine, CA 92697

<sup>‡</sup>Department of Chemistry, Carnegie Mellon University, Pittsburgh, PA 15213

### Abstract

Hydrogen-bonds (H-bonds) within the secondary coordination sphere are often invoked as essential noncovalent interactions that lead to productive chemistry in metalloproteins. Incorporating these types of effects within synthetic systems has proven a challenge in molecular design that often requires the use of rigid organic scaffolds to support H-bond donors or acceptors. We describe the preparation and characterization of a new hybrid tripodal ligand ( $[\text{H}_2\text{pout}]^{3-}$ ) that contains two mono-deprotonated urea groups and one phosphinic amide: the urea groups serve as H-bond donors while the phosphinic amide group serves as a single H-bond acceptor. The  $[\text{H}_2\text{pout}]^{3-}$  ligand was utilized to stabilize a series of Mn-hydroxido complexes in which the oxidation state of the metal center ranges from 2+ to 4+. The molecular structure of  $\text{Mn}^{\text{III}}\text{-OH}$  complex demonstrates that three intramolecular H-bonds involving the hydroxido ligand are formed. Additional evidence for the formation of intramolecular H-bonds was provided by vibrational spectroscopy in which the energy of the O–H vibration supports its assignment as an H-bond donor. The step-wise oxidation of  $[\text{Mn}^{\text{II}}\text{H}_2\text{pout}(\text{OH})]^{2-}$  to its higher oxidized analogs was further substantiated by electrochemical measurements and results from electronic absorbance and electron paramagnetic resonance spectroscopies. Our findings illustrate the utility of controlling both the primary and secondary coordination spheres to achieve structurally similar Mn–OH complexes with varying oxidation states.

### Graphical Abstract

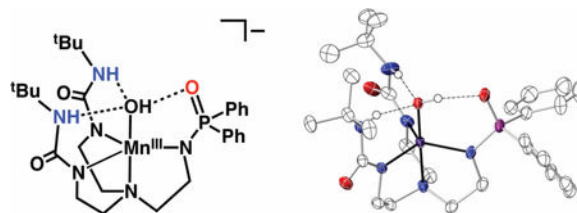
\*Corresponding Author: aborovik@uci.edu.

Supporting Information.

The details for the crystal data (Table S1).

Accession Codes CCDC 1849228–1849229 contain the supplementary crystallographic data for this paper. These data can be obtained free of charge via [www.ccdc.cam.ac.uk/data\\_request/cif](http://www.ccdc.cam.ac.uk/data_request/cif), or by emailing [data\\_request@ccdc.cam.ac.uk](mailto:data_request@ccdc.cam.ac.uk), or by contacting The Cambridge Crystallographic Data Centre, 12 Union Road, Cambridge CB2 1EZ, UK; fax: +44 1223 336033.

The authors declare no competing financial interests.



## Introduction

To determine correlations between the structure and function of a metal complex, it is necessary to understand the relationships between the primary and secondary coordination spheres of the metal ion(s).<sup>1–4</sup> Control of the primary coordination sphere is often governed via relatively strong M–L covalent bonds which chemists have utilized in a variety of ways. Rather than using covalent bonds, the secondary coordination spheres of metal ions are regulated through networks of weaker non-covalent interactions that are often difficult to manipulate within synthetic systems.<sup>5,6</sup> Hydrogen bonds (H-bonds) are the most versatile of these interactions and have been actively designed into a variety of ligand frameworks. The most common of these ligands incorporate either H-bond donors or acceptors to promote intramolecular H-bonds.<sup>3,7–17</sup> However, there are fewer examples that utilize a mixture of H-bond donors/acceptors to target a specific type of M–L unit.<sup>18–21</sup>

Our group has specialized in the development of ligand platforms that promote intramolecular H-bonding networks to investigate their influence on the secondary coordination sphere. One design uses the symmetrical urea ligand [H<sub>3</sub>buea]<sup>3–</sup> (Figure 1A) that provides a cavity with three H-bond donors positioned to stabilize monomeric Mn, Fe, Co, and Ni complexes with terminal oxido/hydroxido ligands.<sup>2,22–28</sup> We found that the strongly anionic ligand field provided by the mono-deprotonated urea groups also assists in stabilizing high valent species that includes Mn<sup>V</sup>-oxido and Mn<sup>IV</sup>-hydroxido complexes.<sup>28–30</sup> We have also examined the chemistry of tripodal ligands such as [RST]<sup>3–</sup> (Figure 1B) which contains deprotonated sulfonamide units that also function as H-bond acceptors.<sup>31–34</sup> Recently, hybrid tripods were introduced that contain both urea and sulfonamido groups to vary the intramolecular H-bonding network that surrounds Co–OH units (Figure 1C).<sup>18</sup> These studies showed that deprotonated sulfonamido ligands are useful H-bond acceptors; however, they do not provide a sufficient primary coordination sphere to stabilize monomeric M–OH complexes with oxidation states greater than 3+.

To circumvent this problem, we have turned to ligands that contain deprotonated phosphinic amides in place of sulfonamido groups. We reasoned that phosphinic amides would produce a stronger anionic ligand field while still providing H-bond acceptors through the P=O units. In this report, we describe the development and Mn chemistry of the hybrid ligand [H<sub>2</sub>pout]<sup>3–</sup> (Figure 2) that installs a combination of two H-bond donors and one H-bond acceptor within the secondary coordination sphere. The [H<sub>2</sub>pout]<sup>3–</sup> ligand was used to prepare the Mn<sup>II</sup>–OH complex [Mn<sup>II</sup>H<sub>2</sub>pout(OH)]<sup>2–</sup> (Figure 2) which had sufficiently low redox potentials to synthetically prepare its corresponding Mn<sup>n</sup>–OH (n = III, IV) analogs.

## Experimental Section

### General Procedures.

All manipulations, unless otherwise stated, were completed under an argon atmosphere in a VAC drybox. Solvents were sparged with argon and dried over columns containing Q-5 and molecular sieves. All reagents were purchased from commercial suppliers and used as received unless otherwise noted. Potassium hydride as a 30% suspension in mineral oil was filtered and washed five times each with Et<sub>2</sub>O and pentane and dried under vacuum. The ligand precursors 1,1'-(((2-aminoethyl)azanediyl)bis(ethane-2,1-diyl))bis(3-(*tert*-butyl)urea) and ferrocenium tetrafluoroborate were synthesized using literature procedures.<sup>10,35</sup>

### Physical Methods.

Electronic absorbance spectra were recorded in a 1 cm cuvette on an 8453 Agilent UV-vis spectrometer equipped with an Unisoku Unispeks cryostat. X-band (9.64 GHz) and S-band (3.50 GHz) EPR spectra were recorded on a Bruker spectrometer equipped with Oxford liquid helium cryostats. The quantification of all signals is relative to a CuEDTA spin standard. The concentration of the standard was derived from an atomic absorption standard (Aldrich). For all instruments, the microwave frequency was calibrated with a frequency counter and the magnetic field with an NMR gaussmeter. A modulation frequency of 100 kHz was used for all EPR spectra. The EPR simulation software (*SpinCount*) was written by one of the authors.<sup>36</sup> EPR samples were prepared under an inert atmosphere, sealed with a septum, and cooled to 77K unless otherwise mentioned. The sign of D for Mn(II)-OH and Mn(IV)-OH were determined from simulations of perpendicular-mode EPR spectra collected at variable temperatures. The sign of D for the Mn(III)-OH complex has not been determined experimentally and is based on the value obtained for the similar complexes, [Mn(III)H<sub>3</sub>buea(OH)]<sup>2-</sup>. <sup>1</sup>H and <sup>13</sup>C nuclear magnetic resonance (NMR) spectroscopies were conducted using a Bruker DRX500 spectrometer. Cyclic voltammetric experiments were conducted using a CHI600C electrochemical analyzer. A 2.0 mm glassy carbon electrode was used as the working electrode at scan velocities of 100 mV s<sup>-1</sup>. A cobaltocenium/cobaltocene couple (CoCp<sub>2</sub><sup>+/0</sup>/CoCp<sub>2</sub>) (E<sub>p</sub> = -0.136 V vs Fc<sup>+/0</sup>) was used to monitor the Ag wire reference electrode, and all potentials are reference to the Fc<sup>+/0</sup> couple. The DFT calculations were performed with Gaussian '09<sup>37</sup> using the hybrid functional B3LYP and the basis set 6-311G. Geometry optimizations were performed using the structures determined from X-ray diffraction for the Mn<sup>II</sup> and Mn<sup>III</sup> complexes. The calculations for the manganese(IV) complex were based on the crystal structure of the Mn<sup>III</sup> complex.

### Preparative Methods.

**H<sub>5</sub>pout.**—The preparative route for this compound followed the method previous report for H<sub>2</sub>2<sup>Tol</sup> in which only the last step was different.<sup>18</sup> A solution of 1,1'-(((2-aminoethyl)azanediyl)bis(ethane-2,1-diyl))bis(3-(*tert*-butyl)urea) (2.00 g, 4.47 mmol) and triethylamine (2.55 g, 25.2 mmol) in 100 mL anhydrous THF was treated dropwise with diphenyl phosphinic chloride dissolved in 100 mL THF (~1 drops/second) while stirring and a white precipitate formed immediately. Once the addition was complete, 100 mL THF was added to rinse the addition funnel. The addition funnel was removed, and the round bottom flask was covered with a glass stopper. After stirring overnight, the white precipitate,

Et<sub>3</sub>NHCl, was removed via filtration. The filtrate was dried under reduced pressure and the solid residue was further dried under vacuum. Diethyl ether (150 mL) was added to the residue to afford an off-white powder, which was collected on a medium porosity glass-fritted funnel, washed once with MeCN (50 mL), twice with Et<sub>2</sub>O (50 mL), and dried for several hours under reduced pressure to give the desired white product (2.7 g, 85 %). <sup>1</sup>H NMR (500 MHz, CDCl<sub>3</sub>, ppm): 2.50 (t, 6H), 3.11 (q, 6H), 6.13 (q, 3H), 7.45 (t, 12H), 7.50 (d, 6H), 7.61 (t, 12H); <sup>13</sup>C NMR (125 MHz, CDCl<sub>3</sub>, ppm): 29.7, 36.3, 45.7, 49.7, 128.9 (d), 130.8, 131.9, 132.0 (d), 132.4 (d), 158.5. <sup>31</sup>P NMR (162 MHz, CDCl<sub>3</sub>, ppm): 28.6; HRMS (ES+, m/z): Exact mass calculated for NaC<sub>42</sub>H<sub>45</sub>N<sub>4</sub>O<sub>9</sub>P<sub>3</sub> [M + Na]: 567.3188, Found: 567.3186. FTIR (Nugol, cm<sup>-1</sup>): 3400, 3341, 3231, 2954, 2922, 2853, 1678, 1657, 1546, 1451, 1378, 1287, 1264, 1221, 1120, 1047, 814, 723, 690.

**K<sub>2</sub>[Mn<sup>II</sup>H<sub>2</sub>pout(OH)].**—A solution of H<sub>5</sub>pout (0.100 g, 0.183 mmol) in anhydrous DMA (4 mL) was treated with potassium hydride (KH) (0.030 g, 0.75 mmol) and the reaction allowed to proceed until gas evolution ceased and all solids were dissolved. To the colorless solution was added Mn<sup>II</sup>(OAc)<sub>2</sub> (0.031 g, 0.18 mmol). After stirring for 90 min, water (3 μL, 0.2 mmol) was added via syringe and the reaction mixture was filtered after 15 min through a medium porosity glass-fritted funnel to afford a light-yellow filtrate and white solid on the glass frit (KOAc, 90%). Et<sub>2</sub>O was allowed to diffuse into DMA resulting in pale yellow crystals (80%) suitable for XRD studies. Anal. Calcd for K<sub>2</sub>[MnH<sub>2</sub>pout(OH)], C<sub>28</sub>H<sub>43</sub>K<sub>2</sub>MnN<sub>6</sub>O<sub>4</sub>P: C, 48.61; H, 6.27; N, 12.15. Found C, 48.79; H, 6.91; N, 12.48. FTIR (ATR, cm<sup>-1</sup>) 3656, 3261, 3124, 3071, 2955, 2797, 1645, 1585, 1510, 1435, 1390, 1350, 1310, 1245, 1205, 1185, 1115, 1045, 1015, 975, 885, 815, 755, 710, 630. UV-vis (DMF:THF, λ<sub>max</sub> nm, (ε<sub>max</sub>, M<sup>-1</sup> cm<sup>-1</sup>)) 525 (sh). EPR (X-band Perpendicular, DMF:THF, 16 K, g = 6.0, 3.9, 2.4, 1.6, 1.4, 1.3, A<sub>iso</sub> = 250). E<sub>1/2</sub> (DMF, V vs [FeCp<sub>2</sub>]<sup>+/-</sup>): Mn<sup>III/II</sup> = -1.47.

**K[Mn<sup>III</sup>H<sub>2</sub>pout(OH)]** was prepared by a similar method to K<sub>2</sub>[Mn<sup>II</sup>H<sub>2</sub>pout(OH)] with the following modifications: after the addition of water, half an equivalent of elemental I<sub>2</sub> (0.028 g, 0.11 mmol) was added to the yellow filtrate that caused an immediately color change to dark green. The solution was left to stir for 30 min and then concentrated to dryness under reduced pressure. The residue was titrated with Et<sub>2</sub>O (20 mL) and again dried under vacuum. The free-flowing green solid was redissolved in MeCN and filtered through a fine porous-glass frit to remove a white solid (KI, 27 mg, 90%). Single crystals suitable for XRD studies were obtained by vapor diffusion of Et<sub>2</sub>O into the solution of DMA of the salt (60%). Anal. Calcd for K<sub>2</sub>[MnH<sub>2</sub>pout(OH)], C<sub>28</sub>H<sub>43</sub>KMnN<sub>6</sub>O<sub>4</sub>P • 0.5KI • DMA: C, 46.71; H, 6.37; N, 11.92. Found C, 46.74; H, 6.38; N, 11.28. FTIR (ATR, cm<sup>-1</sup>) 3300, 3274, 3211, 2956, 2875, 2810, 1610, 1567, 1500, 1490, 1462, 1450, 1433, 1420, 1399, 1378, 1369, 1238, 1112, 1006, 1020, 978, 790, 743, 724, 696, 661, 616, 594. UV-vis (DMF:THF, λ<sub>max</sub> nm, (ε<sub>max</sub>, M<sup>-1</sup> cm<sup>-1</sup>)) 440 (210), 740 (236). EPR (X-band Perpendicular, DMF:THF, 19 K, g = 8, A<sub>Z</sub> = 270) E<sub>0</sub> (DMF, V vs [FeCp<sub>2</sub>]<sup>+/-</sup>): Mn<sup>IV/III</sup> = -0.25.

**Oxidation of [Mn<sup>III</sup>H<sub>2</sub>pout(OH)]<sup>-</sup>.**—A 20 mM stock solution of K[MnH<sub>2</sub>pout(OH)] was prepared in a 1:1 DMF:THF mixture at room temperature and kept in a -35 °C freezer for the duration of the experiment. Addition, via air tight syringe, of a 40 μL aliquot of stock

metal complex to the solvent mixture (2 mL) in a 1 cm quartz cuvette, which was sealed with a rubber septum and precooled to the desired temperature in the 8453 Agilent UV–vis spectrophotometer equipped with an Unisoku Unispeks cryostat, to give the desired concentration for oxidation experiments (400  $\mu\text{M}$ ). The solution of metal complex was allowed to equilibrate to the desired temperature for at least 15 min. Additionally, a stock solution of  $[\text{FeCp}_2]\text{BF}_4$  (40 mM) was prepared in 1:1 DMF:THF mixture and kept in a  $-35\text{ }^\circ\text{C}$  freezer for the duration of the experiment. One equiv (20  $\mu\text{L}$ ) of  $[\text{FeCp}_2]\text{BF}_4$  was added to the  $\text{Mn}^{\text{III}}\text{-OH}$  solution via gastight syringe. The disappearance of the two low-energy d-d transitions corresponding to the  $\text{Mn}^{\text{III}}\text{-OH}$  species were monitored spectrophotometrically, with the appearance of new transitions attributed to the  $\text{Mn}^{\text{IV}}\text{-OH}$  species. EPR samples were prepared in a similar manner and frozen via submersion into liquid  $\text{N}_2$ . The value of D for  $[\text{Mn}^{\text{II}}\text{H}_2\text{pout}(\text{OH})]^{2-}$  and  $[\text{Mn}^{\text{IV}}\text{H}_2\text{pout}(\text{OH})]$  were determined from simulations of EPR spectra collected at variable temperatures. For  $[\text{Mn}^{\text{III}}\text{H}_2\text{pout}(\text{OH})]^-$ , the value of D was determined from the temperature dependence of the signal as displayed in Figure 7.

### X-ray Crystallographic Methods.

A Bruker SMART APEX II diffractometer was used to collect all data. The APEX2<sup>38</sup> program package was used to determine the unit-cell parameters and for data collections. The raw frame data was processed using SAINT<sup>39</sup> and SADABS<sup>40</sup> to yield the reflection data files. Subsequent calculations were carried out using the SHELXTL<sup>40</sup> program. The structures were solved by direct methods and refined on F2 by full-matrix least-squares techniques.

## Results and Discussion

### Synthesis.

The preparation of  $\text{H}_5\text{pout}$  was accomplished in a five-step convergent synthesis adapted from the methods developed for previously reported  $\text{H}_5\mathbf{2}^{\text{tol}}$  ligand (Figure 1C).<sup>18</sup> Central to the syntheses is the diurea compound, 1,1'-((2-aminoethyl)azanediyl)bis(ethane-2,1-diyl)bis(3-(*tert*-butyl)urea) which is combined in the final step with diphenylphosphinic chloride in THF and excess  $\text{Et}_3\text{N}$ . Precipitation of the ammonium chloride salt was observed immediately, and  $\text{H}_5\text{pout}$  was isolated as a white solid in 85% yield after purification.

The  $\text{Mn}^{\text{II}}\text{-OH}$  complex,  $[\text{Mn}^{\text{II}}\text{H}_2\text{pout}(\text{OH})]^{2-}$ , was synthesized following the procedure outline in Scheme 1, in which the ligand was initially formed via deprotonation with KH. Metal ion coordination was achieved using  $\text{Mn}^{\text{II}}(\text{OAc})_2$  and the hydroxido ligand was derived from water; note that an extra equivalent of base was added to the reaction mixture which is needed to produce the hydroxido ligand in  $[\text{Mn}^{\text{II}}\text{H}_2\text{pout}(\text{OH})]^{2-}$ . One-electron oxidation of the  $\text{Mn}^{\text{II}}\text{-OH}$  complex with elemental iodine gave the corresponding  $\text{Mn}^{\text{III}}\text{-OH}$  species,  $[\text{Mn}^{\text{III}}\text{H}_2\text{pout}(\text{OH})]^-$  (Scheme 1).<sup>26</sup>

### Structural Properties.

The molecular structures of  $\text{K}_2[\text{Mn}^{\text{II}}\text{H}_2\text{pout}(\text{OH})]$  and  $\text{K}[\text{Mn}^{\text{III}}\text{H}_2\text{pout}(\text{OH})]$  salts were characterized with X-ray diffraction methods (Figure 3, Tables 1 and 2). DFT calculations

gave optimized structures for both that agreed with the molecular structures determined by XRD measurements (Table 1). The structures for both salts revealed that each Mn–OH anion is mononuclear with a distorted trigonal bipyramidal (tbp) coordination geometries. The primary coordination spheres around the Mn center in each complex is composed of a N<sub>4</sub>O donor set with three anionic N-atom donors forming the trigonal plane. The axial positions contain the apical amine N1-atom from the [H<sub>2</sub>pout]<sup>3-</sup> ligand and O1-atom from the hydroxido ligand. Statistically significant differences are found between the Mn–N and Mn–O1 bond lengths between the two structures. For instance, the Mn–O1 bond distance is contracted from 2.051(1) Å to 1.834(1) Å upon conversion to [Mn<sup>III</sup>H<sub>2</sub>pout(OH)]<sup>-</sup>, a change which is consistent with oxidation at the metal center. A similar shortening in bond lengths after oxidation is observed for the bonds within the equatorial plane, in which the average Mn–N bond distance changed from 2.188(1) Å to 2.052(2) Å.

The molecular structures also show that [H<sub>2</sub>pout]<sup>3-</sup> interacts with the Mn–OH unit through H-bonds to influence the secondary coordination sphere. In each structure, the urea NH groups serve as H-bond donors to the hydroxido ligand as judged by the average N...O distances of 2.910(2) Å in [Mn<sup>II</sup>H<sub>2</sub>pout(OH)]<sup>2-</sup> and 2.774(2) Å in [Mn<sup>III</sup>H<sub>2</sub>pout(OH)]<sup>-</sup>. There is a third intramolecular H-bond in the Mn<sup>III</sup>–OH structure that is formed between the hydroxido ligand and the O2-atom of the phosphinic group (2.685(2) Å). The presence of this additional H-bond could account for the shorter Mn–O bond distance in [Mn<sup>III</sup>H<sub>2</sub>pout(OH)]<sup>-</sup> when compared to that found in [Mn<sup>III</sup>H<sub>3</sub>buea(OH)]<sup>-</sup> (Figure 1A, Mn–O bond length of 1.877(2) Å).<sup>41</sup> Because the hydroxido acts as an H-bond donor, it should have more negative character, which would result in a shorter Mn1–O1 bond distance in [Mn<sup>III</sup>H<sub>2</sub>pout(OH)]<sup>-</sup>. Similar structural results were found in Co–OH complexes and emphasized the structural effects of the H-bonds within the secondary coordination sphere.<sup>18</sup> Notice also potassium ion does not interact with the Mn–OH unit in the lattice of K[Mn<sup>III</sup>H<sub>2</sub>pout(OH)]; it only interact with the carbonyl groups of the ureas which are pointed away from the hydroxido ligand (Figure 3D).

Similar comparison for [Mn<sup>II</sup>H<sub>2</sub>pout(OH)]<sup>2-</sup> are hindered because the positioning of the potassium ions complicates interpretation of the secondary coordination sphere. One potassium ion (K2) interacts with the O2-atom of [H<sub>2</sub>pout]<sup>3-</sup> that distorts the cavity and prevents formation of an intramolecular H-bond (Figure 3B). However, the O–H bond is positioned toward the phosphinic unit in a similar manner as in [Mn<sup>III</sup>H<sub>2</sub>pout(OH)]<sup>-</sup>, but it is now closer to one of the phenyl substituents. This lack of a third intramolecular H-bonds results in a Mn1–O1 bond length that is the statistically the same as that found in the related Mn<sup>II</sup>–OH complex, [Mn<sup>II</sup>H<sub>3</sub>buea(OH)]<sup>2-</sup> (Mn–O bond distance of 2.059(2) Å).<sup>26</sup>

### Electronic Absorbance and Vibrational Properties.

The conversion of [Mn<sup>II</sup>H<sub>2</sub>pout(OH)]<sup>2-</sup> to [Mn<sup>III</sup>H<sub>2</sub>pout(OH)]<sup>-</sup> was monitored by optical spectroscopy in 1:1 DMF:THF at –80°C. The Mn<sup>II</sup>–OH species had no observable features in the visible region but upon oxidation new bands appeared at λ<sub>max</sub>(ε<sub>M</sub>) = 440 (210) and 740 (236) nm (Figure 4A). The energies of these features are similar to those found in the related Mn<sup>III</sup>–O(H) complexes [Mn<sup>III</sup>H<sub>3</sub>buea(O)]<sup>2-</sup> and [Mn<sup>III</sup>H<sub>3</sub>buea(OH)]<sup>-</sup>; however, there are noticeable differences in the values of the extension coefficients. For



$[\text{Mn}^{\text{III}}\text{H}_3\text{buea}(\text{OH})]^-$ , bands were observed at  $\lambda_{\text{max}}(\epsilon_{\text{M}}) = 427$  ( $\epsilon_1 = 390$ ) and  $720$  ( $\epsilon_2 = 500$ ) nm ( $\epsilon_1/\epsilon_2 = 0.78$ ) that change in  $[\text{Mn}^{\text{III}}\text{H}_3\text{buea}(\text{O})]^{2-}$  to  $\lambda_{\text{max}}(\epsilon_{\text{M}}) = 498$  ( $\epsilon_1 = 490$ ) and  $725$  ( $\epsilon_2 = 240$ ) nm ( $\epsilon_1/\epsilon_2 = 2.0$ ).<sup>42</sup> In addition, an analogous  $\text{Mn}^{\text{III}}\text{-OH}$  in *tbp* coordination geometry with no intramolecular H-bonds has a similar visible absorbance spectrum in which the lower energy band has the greater intensity ( $\epsilon_1/\epsilon_2 = 0.62$ ).<sup>43</sup> The comparable extinction coefficients of the absorbance bands in the spectrum of  $[\text{Mn}^{\text{III}}\text{H}_2\text{pout}(\text{OH})]^-$  ( $\epsilon_1/\epsilon_2 = 0.89$ ) may be attributed to the Mn–OH unit being an H-bond donor to form a relatively strong H-bond with the phosphinic amide O-atom; this additional interaction would make the hydroxido ligand slightly more oxido-like, which would affect a change in the absorbance spectrum as observed.

Analysis of vibrational properties using FTIR spectroscopy showed bands attributed to the  $\nu(\text{MnO-H})$  at  $3656$  and  $3300$   $\text{cm}^{-1}$  for the  $\text{Mn}^{\text{II}}\text{-OH}$  and  $\text{Mn}^{\text{III}}\text{-OH}$  complexes. Because of the interactions of the potassium ions with  $[\text{Mn}^{\text{II}}\text{H}_2\text{pout}(\text{OH})]^{2-}$  (Figure 3A) it is not possible to directly compare this complex with other Mn–OH species. A more straightforward comparison can be made for  $[\text{Mn}^{\text{III}}\text{H}_2\text{pout}(\text{OH})]^-$  and its  $\nu(\text{MnO-H})$  band is broader (fwhm =  $90$   $\text{cm}^{-1}$ ) and at lower energy than the comparable peak for  $[\text{Mn}^{\text{III}}\text{H}_3\text{buea}(\text{OH})]^-$  which was found at  $3613$   $\text{cm}^{-1}$  (fwhm =  $15$   $\text{cm}^{-1}$ ).<sup>41</sup> These vibrational data are also consistent with presence of an intramolecular H-bond between the phosphinic arm and the hydroxido ligand that causes a weaken the O–H bond.

### Electrochemical Properties.

Cyclic voltammetry (CV) was employed to analyze the redox properties of the Mn–OH complexes. Electrochemical data showed a reversible one-electron redox couple at  $-1.47$  V vs  $[\text{FeCp}_2]^{+/0}$  that is assigned to the  $\text{Mn}^{\text{III/II}}\text{-OH}$  process (Figure 5B). This potential is similar to one found in  $[\text{Mn}^{\text{III}}\text{H}_3\text{buea}(\text{OH})]^-$  that occurs at  $-1.50$  V vs  $[\text{FeCp}_2]^{+/0}$  that is the  $\text{Mn}^{\text{III/II}}\text{ OH}$  couple.<sup>44</sup> A second redox event was observed at a more positive potential that is centered around  $-0.25$  V vs  $[\text{FeCp}_2]^{+/0}$  and assigned to the  $\text{Mn}^{\text{IV/III}}\text{-OH}$  couple (Figure 5B).

The process is not reversible under our experimental conditions which we suggest is caused by the oxidized  $\text{Mn}^{\text{IV}}\text{-OH}$  species not being stable at room temperature. Again, a similar result was observed for the  $\text{Mn}^{\text{IV/III}}\text{-OH}$  couple ( $-0.18$  V vs  $[\text{FeCp}_2]^{+/0}$ ) for  $[\text{Mn}^{\text{IV}}\text{H}_3\text{buea}(\text{OH})]$  at room temperature and subsequent studies found it was only stable at temperatures lower than  $-50^\circ\text{C}$ .<sup>30</sup>

### Accessing a $\text{Mn}^{\text{IV}}\text{-OH}$ Species: Spectroscopic Studies.

The electrochemical data of the  $\text{Mn}^{\text{II}}\text{-OH}$  complex suggested that accessing a higher valent  $\text{Mn}^{\text{IV}}\text{-OH}$  species should be possible with mild oxidants. We tested this premise by monitoring the formation of this complex at  $-80^\circ\text{C}$  in 1:1 DMF:THF mixture using ferrocenium cation as the oxidant. Clean conversion was observed that initiated from  $[\text{Mn}^{\text{III}}\text{H}_3\text{buea}(\text{OH})]^-$  to produce a new spectrum with a prominent band at  $\lambda_{\text{max}}(\epsilon_{\text{M}}) = 460$  nm ( $1390$ ) and a shoulder at  $560$  nm; a single isosbestic point was found at  $675$  nm (Figure 4B). The final spectrum closely resembled that of  $[\text{Mn}^{\text{IV}}\text{H}_3\text{buea}(\text{OH})]$  which has an absorbance band  $\lambda_{\text{max}}(\epsilon_{\text{M}}) = 466$  nm ( $5600$ ). This new oxidized species was stable for hours at  $-80^\circ\text{C}$ .



## EPR Studies.

We have previously shown that EPR spectroscopy is an effective method for probing changes in the electronic structure of monomeric Mn–O(H) complexes.<sup>30</sup> Our approach utilized both perpendicular- and parallel-modes at X-band to follow spin state changes upon oxidation (Table 2). The EPR spectrum of  $[\text{Mn}^{\text{II}}\text{H}_2\text{pout}(\text{OH})]^{2-}$  (Figure 6) in perpendicular-mode showed signals over a wide magnetic field range. The spectra are complicated by resonances from multiple overlapping transitions as has been described previously for  $[\text{Mn}^{\text{II}}\text{H}_3\text{buea}(\text{OH})]^{2-}$ .<sup>45</sup> The simulation overlaid on the experimental spectrum in Figure 6 is for a  $S = 5/2$  spin center using the parameters of described in Table 2. The simulation intensity is in quantitative agreement with the sample concentration determined from the weight of the complex dissolved in the solvent. The zero-field parameters are similar to the previously characterized  $[\text{Mn}^{\text{II}}\text{H}_3\text{buea}(\text{OH})]^{2-}$  and, as expected,  $[\text{Mn}^{\text{II}}\text{H}_2\text{pout}(\text{OH})]^{2-}$  showed an increased in rhombic parameter  $E/D$  owing to the unsymmetrical nature of the tripodal ligand.<sup>45</sup>

The addition of 1 equiv  $[\text{Fe}^{\text{III}}\text{Cp}_2]^+$  resulted in the disappearance of the signals from the  $\text{Mn}^{\text{II}}\text{–OH}$  complex and the appearance of a 6-line hyperfine signal centered at  $g = 8$  with  $A_z = 270$  MHz ( $a = 9.6$  mT) in parallel-mode (Figure 7). The simulation overlaid on the experimental spectrum are for an  $S = 2$  spin center (Figure 7, Table 2) and its intensity is in quantitative agreement with the sample concentration. The zero-field parameters determined from the spectra are statistically the same as those of  $[\text{Mn}^{\text{III}}\text{H}_3\text{buea}(\text{OH})]^-$ .<sup>45</sup> Taken together, these data are consistent with the formation of the high-spin  $\text{Mn}^{\text{III}}\text{–OH}$  complex,  $[\text{Mn}^{\text{III}}\text{H}_2\text{pout}(\text{OH})]^-$ .

The fully oxidized  $[\text{Mn}^{\text{IV}}\text{H}_2\text{pout}(\text{OH})]$  complex showed no features in parallel-mode, but perpendicular-mode signals were observed when measured at both S- and X-bands. Figure 8 displaces the spectra collected at both bands with the magnetic field ranges chosen to equate the  $g$ -value ranges for both frequencies. The positions of the resonances and the simulations are indicative of an  $S = 3/2$  spin-state that is consistent with a high-spin  $\text{Mn}^{\text{IV}}\text{–OH}$  complex in local  $C_3$  symmetry (Table 2). Our analysis of the EPR data showed that two distinct  $\text{Mn}^{\text{IV}}\text{–OH}$  species are formed, a result that is similar to what we reported for  $[\text{Mn}^{\text{IV}}\text{H}_3\text{buea}(\text{OH})]$ .<sup>30,45</sup> The largest difference between the two species for  $[\text{Mn}^{\text{IV}}\text{H}_2\text{pout}(\text{OH})]$  is in their  $E/D$  values: species 1 ( $E/D = 0.33$ ) is significantly more rhombic than species 2 ( $E/D = 0.17$ ). The effective  $g$ -tensors for the  $|\pm 1/2\rangle$  and excited  $|\pm 3/2\rangle$  doublets for the two species are reported in Table 3 and indicated on Figure 8. For species 1, the effective  $g$ -tensors for each doublet are the same because of the large value of  $E/D$ . We have been successful in determining the hyperfine tensor for both species, even though the hyperfine splitting is not resolved in all directions. This determination was accomplished because we used two different frequencies in our analysis as previously described.<sup>28</sup>

The rhombic character of the two species is consistent with a  $\text{Mn}^{\text{IV}}$  ion in a  $C_3$  symmetry in which an appreciable Jahn-Teller distortion is expected. However, the reason(s) for the presence of two species and their exact structural differences are not known. The simulations showed that species 2 (the less rhombic species) was more abundant by a ratio of 2:1. We used density functional theory (DFT) to probe the possible structures of  $[\text{Mn}^{\text{IV}}\text{H}_2\text{pout}(\text{OH})]$ .

The DFT calculations converged to two optimized structures shown in Figures 9 and S1 with selected bond lengths given in Table 3. Structure **A** had a lower energy and is similar to the structure of  $[\text{Mn}^{\text{III}}\text{H}_2\text{pout}(\text{OH})]^-$  with three intramolecular H-bonds involving the hydroxido ligand. Structure **B** has one urea arm rotated such that the carbonyl O-atom was proximal to the Mn–O(H) unit. A similar reorientation of a urea arm has been proposed for the protonated form of  $[\text{Fe}^{\text{IV}}\text{H}_3\text{buea}(\text{O})]^-$ .<sup>46</sup> The computed equatorial Mn–N bond lengths were more similar for species **A** relative to those found for species **B** which suggests **A** corresponds to the species with *E/D* values of 0.17 and 0.33, respectively. DFT calculations of the spin-dipolar A-tensors for the two species gave (29, –2, –27) MHz (**A**) and (30, 6, –36) MHz (**B**), which were in approximate agreement with the experimental values of (17, 3, –20) MHz for **A** and (26, –5, –21) MHz for **B**. Finally, we note that the EPR spectrum of the related complex  $[\text{Mn}^{\text{IV}}\text{H}_3\text{buea}(\text{OH})]^-$  also consisted of two species with similar values for *E/D* to that of  $[\text{Mn}^{\text{IV}}\text{H}_2\text{pout}(\text{OH})]^-$ . However, one important difference between the two  $\text{Mn}^{\text{IV}}\text{–OH}$  complexes is that the more abundant species in  $[\text{Mn}^{\text{IV}}\text{H}_3\text{buea}(\text{OH})]^-$  is the one that is most rhombic (*E/D* = 0.33). The reason(s) for this difference is under investigation.

### Preparation and Properties of $[\text{Mn}^{\text{III}}\text{H}_2\text{pout}(\text{O})]^{2-}$ and $[\text{Mn}^{\text{IV}}\text{H}_2\text{pout}(\text{O})]^-$ .

We have also prepared the related  $\text{Mn}^{\text{III/IV}}\text{–oxido}$  complexes of  $[\text{H}_2\text{pout}]^{2-}$  to compare their spectroscopic properties to the related Mn–OH complexes. The synthesis of  $[\text{Mn}^{\text{III}}\text{H}_2\text{pout}(\text{O})]^{2-}$  was achieved via deprotonation of the  $\text{Mn}^{\text{III}}\text{–OH}$  complex with  $\text{KO}^t\text{Bu}$  (Scheme 2A). Conversion to its  $\text{Mn}^{\text{IV}}\text{–oxido}$  analog was accomplished using ferrocenium (Scheme 2B);  $[\text{Mn}^{\text{IV}}\text{H}_2\text{pout}(\text{O})]^-$  was also prepared via deprotonation of  $[\text{Mn}^{\text{IV}}\text{H}_2\text{pout}(\text{OH})]$  with  $\text{KO}^t\text{Bu}$  (Scheme 2C). The electronic absorbance spectrum of  $[\text{Mn}^{\text{III}}\text{H}_2\text{pout}(\text{O})]^{2-}$  contains two major features in the visible region at  $\lambda_{\text{max}}(\epsilon_{\text{M}}) = 500$  (400) and 760 (190) nm with an  $\epsilon_1/\epsilon_2 = 2.1$  (Figure S2A). These values are reminiscent of those observed for  $[\text{Mn}^{\text{III}}\text{H}_3\text{buea}(\text{O})]^{2-}$  (see above). In addition, the parallel-mode EPR spectrum for  $[\text{Mn}^{\text{III}}\text{H}_2\text{pout}(\text{O})]^{2-}$  showed a six-lined signal at  $g = 7.91$  with a hyperfine constant  $A_z = 290$  MHz that consistent with a monomeric  $\text{Mn}^{\text{III}}$  complex having an  $S = 2$  spin ground state (Figure S3A). Moreover, these values are distinct from those observed for  $[\text{Mn}^{\text{III}}\text{H}_2\text{pout}(\text{OH})]^-$ . Similar differences were observed for  $[\text{Mn}^{\text{IV}}\text{H}_2\text{pout}(\text{O})]^-$  when compared to  $[\text{Mn}^{\text{IV}}\text{H}_2\text{pout}(\text{OH})]$ : the  $\text{Mn}^{\text{IV}}\text{–oxido}$  complex had absorbance bands at  $\lambda_{\text{max}}(\epsilon_{\text{M}}) = 440$  (1060) and 745 (200) nm (Figure S2B) that are similar to those found for  $[\text{Mn}^{\text{IV}}\text{H}_3\text{buea}(\text{O})]^-$ . The perpendicular-mode EPR spectrum of  $[\text{Mn}^{\text{IV}}\text{H}_2\text{pout}(\text{O})]^-$  was broad and only the resonance at  $g = 5.09$  could be identified (Figure S3B). The hyperfine pattern at  $g = 5.09$  and the other broad features were different from that of  $[\text{Mn}^{\text{IV}}\text{H}_2\text{pout}(\text{OH})]$  (Figure S3B). Taken together, these findings demonstrate that the spectroscopic differences between Mn–hydroxido and Mn–oxido complexes with tripodal ligands can be used to differentiate these types of complexes in solution.

### Summary and Conclusions

Manganese complexes with terminal hydroxido ligands are relatively rare because of the strong propensity of the Mn–OH units to aggregate to form multinuclear species. However, they have been implicated as key intermediates in a variety of chemical processes,<sup>26,30,41,43,44,47–54</sup> most notably as intermediates formed during biological water oxidation.

17,55–59 Results from structural biology on the oxygen evolving complex (OEC) suggest that H-bonding networks to coordinate water molecules assist in forming Mn–OH complexes that can be in either the Mn<sup>III</sup> or Mn<sup>IV</sup> oxidation states.<sup>60–64</sup> One approach toward studying the structural outcomes of the secondary coordination sphere is to develop chelating ligands that can provide H-bond donors/accepts around the Mn–OH unit. Toward this goal, tripodal ligand [H<sub>2</sub>pout]<sup>3-</sup> was designed to accommodate three intramolecular H-bond to the hydroxido ligand. Spectroscopic and structural results on [Mn<sup>II</sup>H<sub>2</sub>pout(OH)]<sup>2-</sup> and [Mn<sup>III</sup>H<sub>2</sub>pout(OH)]<sup>-</sup> indicate that this type of H-bonding network was achieved and the O-atom of the phosphinic amide arm can serve as a H-bond acceptor. In addition, our electrochemical studies demonstrate that [Mn<sup>III</sup>H<sub>2</sub>pout(OH)]<sup>-</sup> can be converted to its Mn<sup>IV</sup>–OH analog which was achieved using the mild oxidant ferrocenium. The formation of [Mn<sup>IV</sup>H<sub>2</sub>pout(OH)] was monitored spectrophotometrically and further characterized using variable frequency EPR spectroscopy that showed a high-spin Mn<sup>IV</sup> species is readily formed. These results illustrate the utility of this ligand design in forming mononuclear metal-hydroxido complexes that span a variety of different oxidation states.

## Supplementary Material

Refer to Web version on PubMed Central for supplementary material.

## ACKNOWLEDGMENT

We thank the National Institutes of Health USA (GM050781 to ASB and GM077387 to MPH) for financial support

## REFERENCES

- (1). Shook RL; Borovik AS The Effects of Hydrogen Bonds on Metal-Mediated O<sub>2</sub> activation and Related Processes. *Chem. Commun* 2008, 46, 6095–6107.
- (2). MacBeth CE; Hammes BS; Young VG; Borovik AS; Young VG; Borovik AS Hydrogen-Bonding Cavities about Metal Ions: Synthesis, Structure, and Physical Properties for a Series of Monomeric M–OH Complexes Derived from Water. *Inorg. Chem* 2001, 40, 4733–4741.
- (3). Borovik AS Bioinspired Hydrogen Bond Motifs in Ligand Design: The Role of Noncovalent Interactions in Metal Ion Mediated Activation of Dioxygen. *Acc. Chem. Res* 2005, 38, 54–61. [PubMed: 15654737]
- (4). Shook RL; Borovik AS Role of the Secondary Coordination Sphere in Metal-Mediated Dioxygen Activation. *Inorg. Chem* 2010, 49, 3646–3660. [PubMed: 20380466]
- (5). Cook SA; Hill EA; Borovik AS Lessons from Nature: A Bio-Inspired Approach to Molecular Design. *Biochemistry* 2015, 54, 4167–4180. [PubMed: 26079379]
- (6). Cook SA; Borovik AS Molecular Designs for Controlling the Local Environments around Metal Ions. *Acc. Chem. Res* 2015, 48, 2407–2414. [PubMed: 26181849]
- (7). Szymczak NK; Oelkers AB; Tyler DR Detection of Hydrogen Bonding in Solution: A <sup>2</sup>H Nuclear Magnetic Resonance Method Based on Rotational Motion of a Donor/Acceptor Complex. *Phys. Chem. Chem. Phys* 2006, 8, 4002–4008. [PubMed: 17028690]
- (8). Hartle MD; Delgado M; Gilbertson JD; Pluth MD Stabilization of a Zn(II) Hydrosulfido Complex Utilizing a Hydrogen-Bond Accepting Ligand. *Chem. Commun* 2016, 52, 7680–7682.
- (9). Dahl EW; Dong HT; Szymczak NK Phenylamino Derivatives of Tris(2-Pyridylmethyl)Amine: Hydrogen-Bonded Peroxodicopper Complexes. *Chem. Commun* 2018, 54, 892–895.
- (10). Lucas RL; Zart MK; Murkerjee J; Sorrell TN; Powell DR; Borovik AS A Modular Approach toward Regulating the Secondary Coordination Sphere of Metal Ions: Differential Dioxygen

- Activation Assisted by Intramolecular Hydrogen Bonds. *J. Am. Chem. Soc* 2006, 128, 15476–15489. [PubMed: 17132015]
- (11). Kendall AJ; Zakharov LN; Gilbertson JD Synthesis and Stabilization of a Monomeric Iron(II) Hydroxo Complex via Intra Molecular Hydrogen Bonding in the Secondary Coordination Sphere. *Inorg. Chem* 2010, 49, 8656–8658. [PubMed: 20799715]
- (12). Dauth A; Love JA Synthesis and Reactivity of 2-Azametallacyclobutanes. *Dalton Trans* 2012, 41, 7782–7791. [PubMed: 22609770]
- (13). Lacy DC; Mukherjee J; Lucas RL; Day VW; Borovik AS Metal Complexes with Varying Intramolecular Hydrogen Bonding Networks. *Polyhedron* 2013, 52, 261–267. [PubMed: 24904193]
- (14). Moore CM; Szymczak NK 6,6'-Dihydroxy Terpyridine: A Proton-Responsive Bifunctional Ligand and Its Application in Catalytic Transfer Hydrogenation of Ketones. *Chem. Commun* 2013, 49, 400–402.
- (15). Matson EM; Bertke JA; Fout AR Isolation of Iron(II) Aqua and Hydroxyl Complexes Featuring a Tripodal H-Bond Donor and Acceptor Ligand. *Inorg. Chem* 2014, 53, 4450–4458. [PubMed: 24758308]
- (16). Matson EM; Park YJ; Fout AR Facile Nitrite Reduction in a Non-Heme Iron System: Formation of an Iron(III)-Oxo. *J. Am. Chem. Soc* 2014, 136, 17398–17401. [PubMed: 25470029]
- (17). Li X; Siegbahn PEM Alternative Mechanisms for O<sub>2</sub> Release and O–O Bond Formation in the Oxygen Evolving Complex of Photosystem II. *Phys. Chem. Chem. Phys* 2015, 17, 12168–12174. [PubMed: 25879997]
- (18). Jones JR; Ziller JW; Borovik AS Modulating the Primary and Secondary Coordination Spheres within a Series of Co<sup>II</sup>-OH Complexes. *Inorg. Chem* 2017, 56, 1112–1120. [PubMed: 28094522]
- (19). Matson EM; Bertke JA; Fout AR Isolation of Iron(II) Aqua and Hydroxyl Complexes Featuring a Tripodal H-Bond Donor and Acceptor Ligand. *Inorg. Chem* 2014, 53, 4450–4458. [PubMed: 24758308]
- (20). Park YJ; Matson EM; Nilges MJ; Fout AR Exploring Mn-O Bonding in the Context of an Electronically Flexible Secondary Coordination Sphere: Synthesis of a Mn(III)-Oxo. *Chem. Commun* 2015, 51, 5310–5313.
- (21). Matson EM; Park YJ; Fout AR Facile Nitrite Reduction in a Non-Heme Iron System: Formation of an Iron(III)-Oxo. *J. Am. Chem. Soc* 2014, 136, 17398–17401. [PubMed: 25470029]
- (22). Ray M; Golombek AP; Hendrich MP; Young VG; Borovik AS Synthesis and Structure of a Trigonal Monopyramidal Fe(II) Complex and Its Paramagnetic Carbon Monoxide Derivative. *J. Am. Chem. Soc* 1996, 118, 6084–6085.
- (23). Hammes BS; Ramos-Maldonado D; Yap GPA; Liable-Sands L; Rheingold AL; Young VG; Borovik AS C<sub>3</sub>-Symmetric Chiral Amidate Complexes: Effects of Ligand Binding on Cavity Structure. *Inorg. Chem* 1997, 36, 3210–3211. [PubMed: 11669981]
- (24). Hammes BS; Young VG, Jr.; Borovik AS Hydrogen-Bonding Cavities about Metal Ions: A Redox Pair of Coordinatively Unsaturated Paramagnetic Co-OH Complexes. *Angew. Chem. Int. Ed* 1999, 38, 666–669.
- (25). Shirin Z; Hammes BS; Young VG; Borovik AS Hydrogen Bonding in Metal Oxo Complexes: Synthesis and Structure of a Monomeric Manganese(III)-Oxo Complex and Its Hydroxo Analogue. *J. Am. Chem. Soc* 2000, 122, 1836–1837.
- (26). Gupta R; MacBeth CE; Young VGJ; Borovik AS Isolation of Monomeric Mn<sup>III/II</sup>-OH and Mn<sup>III</sup>-O Complexes from Water: Evaluation of O-H Bond Dissociation Energies. *J. Am. Chem. Soc* 2002, 124, 1136–1137. [PubMed: 11841259]
- (27). Gupta R; Borovik AS Monomeric Mn<sup>III/II</sup> and Fe<sup>III/II</sup> Complexes with Terminal Hydroxo and Oxo Ligands: Probing Reactivity via O–H Bond Dissociation Energies. *J. Am. Chem. Soc* 2003, 125, 13234–13242. [PubMed: 14570499]
- (28). Gupta R; Taguchi T; Lassalle-Kaiser B; Bominaar EL; Yano J; Hendrich MP; Borovik AS High-Spin Mn–Oxo Complexes and Their Relevance to the Oxygen-Evolving Complex within Photosystem II. *Proc. Natl. Acad. Sci* 2015, 112, 5319–5324. [PubMed: 25852147]





- (49). Leto DF; Massie AA; Colmer HE; Jackson TA X-Band Electron Paramagnetic Resonance Comparison of Mononuclear Mn<sup>IV</sup>-Oxo and Mn<sup>IV</sup>-Hydroxo Complexes and Quantum Chemical Investigation of Mn<sup>IV</sup> Zero-Field Splitting. *Inorg. Chem* 2016, 55, 3272–3282. [PubMed: 27002928]
- (50). Rice DB; Massie AA; Jackson TA Manganese-Oxygen Intermediates in OO Bond Activation and Hydrogen-Atom Transfer Reactions. *Acc. Chem. Res* 2017, 50, 2706–2717. [PubMed: 29064667]
- (51). Wijeratne GB; Corzine B; Day VW; Jackson TA Saturation Kinetics in Phenolic O-H Bond Oxidation by a Mononuclear Mn(III)-OH Complex Derived from Dioxygen. *Inorg. Chem* 2014, 53, 7622–7634. [PubMed: 25010596]
- (52). Coggins MK; Brines LM; Kovacs JA Synthesis and Structural Characterization of a Series of Mn<sup>III</sup>OR Complexes, Including a Water-Soluble Mn<sup>III</sup>OH That Promotes Aerobic Hydrogen-Atom Transfer. *Inorg. Chem* 2013, 52, 12383–12393. [PubMed: 24156315]
- (53). Pal S; Armstrong WH Products from Reactions of Manganese Oxo Complex [Mn<sub>2</sub>O<sub>2</sub>(O<sub>2</sub>CCH<sub>3</sub>)(Tpen)]<sub>2</sub>+ in Acidic and Neutral Aqueous Media: [Mn<sub>2</sub>(μ-O)<sub>2</sub>(μ-O<sub>2</sub>CCH<sub>3</sub>)(Tpen)]<sub>3</sub>+ and [Mn<sub>3</sub>(μ-O)<sub>4</sub>(OH)(Tpen)]<sub>2</sub>(μ-Tpen)]<sub>6</sub>+. *Inorg. Chem* 1992, 31, 5417–5423.
- (54). Goldsmith CR; Cole AP; Stack TDP C-H Activation by a Mononuclear Manganese(III) Hydroxide Complex: Synthesis and Characterization of a Manganese-Lipoxygenase Mimic *J. Am. Chem. Soc* 2005, 127, 9904–9912. [PubMed: 15998097]
- (55). Sproviero EM; Gascon JA; McEvoy JP; Brudvig GW; Batista VS Computational Studies of the O<sub>2</sub>-Evolving Complex of Photosystem II and Biomimetic Oxomanganese Complexes. *Coord. Chem. Rev* 2008, 252, 395–415. [PubMed: 19190716]
- (56). Siegbahn PEM Mechanisms for Proton Release during Water Oxidation in the S<sub>2</sub> to S<sub>3</sub> and S<sub>3</sub> to S<sub>4</sub> Transitions in Photosystem II. *Phys. Chem. Chem. Phys* 2012, 14, 4849. [PubMed: 22278436]
- (57). Siegbahn PEM A Structure-Consistent Mechanism for Dioxygen Formation in Photosystem II. *Chem. Eur. J* 2008, 14, 8290–8302. [PubMed: 18680116]
- (58). Rapatskiy L; Cox N; Savitsky A; Ames WM; Sander J; Nowaczyk MM; Rögner M; Boussac A; Neese F; Messinger J; et al. Detection of the Water-Binding Sites of the Oxygen-Evolving Complex of Photosystem II Using W-Band <sup>17</sup>O Electron-Electron Double Resonance-Detected NMR Spectroscopy. *J. Am. Chem. Soc* 2012, 134, 16619–16634. [PubMed: 22937979]
- (59). Meyer TJ; Huynh MHV; Thorp HH The Possible Role of Proton-Coupled Electron Transfer (PCET) in Water Oxidation by Photosystem II. *Angew. Chem. Int. Ed* 2007, 46, 5284–5304.
- (60). Suga M; Akita F; Hirata K; Ueno G; Murakami H; Nakajima Y; Shimizu T; Yamashita K; Yamamoto M; Ago H; et al. Native Structure of Photosystem II at 1.95 Å Resolution Viewed by Femtosecond X-Ray Pulses. *Nature* 2014, 517, 1–17.
- (61). Pantazis DA; Ames W; Cox N; Lubitz W; Neese F Two Interconvertible Structures That Explain the Spectroscopic Properties of the Oxygen Evolving Complex of Photosystem II in the S<sub>2</sub> State. *Angew. Chem., Int. Ed. Engl* 2012, 51, 9935–9940. [PubMed: 22907906]
- (62). Umena Y; Kawakami K; Shen J-R; Kamiya N Crystal Structure of Oxygen-Evolving Photosystem II at a Resolution of 1.9 Å. *Nature* 2011, 473, 55–60. [PubMed: 21499260]
- (63). Siegbahn PEM Structures and Energetics for O<sub>2</sub> Formation in Photosystem II. *Acc. Chem. Res* 2009, 42, 1871–1880. [PubMed: 19856959]
- (64). Shoji M; Isobe H; Nakajima T; Shigeta Y; Suga M; Akita F; Shen J-R; Yamaguchi K Large-Scale QM/MM Calculations of the CaMn<sub>4</sub>O<sub>5</sub> Cluster in the S<sub>3</sub> State of the Oxygen Evolving Complex of Photosystem II. Comparison between Water-Inserted and No Water-Inserted Structures. *Faraday Discuss* 2017, 198, 83–106. [PubMed: 28276543]

### Synopsis

A new hybrid tripodal ligand led to a series of mononuclear Mn–OH complexes. The ligand framework was tailor to promote three intramolecular hydrogen bonds to the hydroxido ligand: two utilize urea groups as hydrogen bond donors and the third is a phosphinic amide that is a hydrogen bond acceptor. The step-wise oxidation from Mn<sup>II</sup>–OH to Mn<sup>IV</sup>–OH was achieved through control of the primary and secondary coordination spheres.



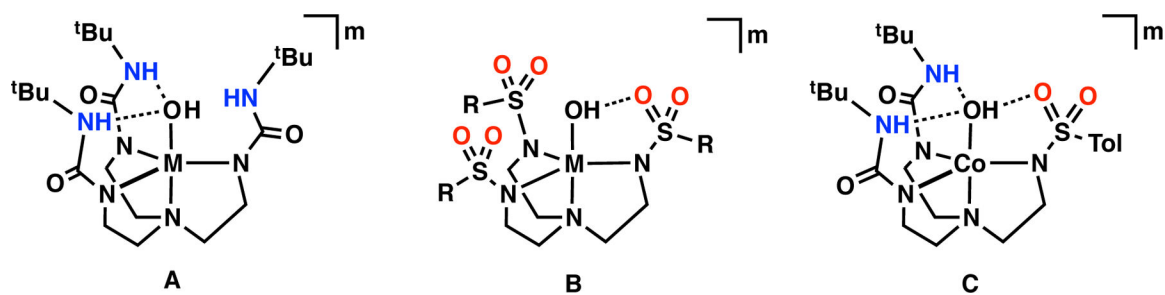


**Figure 1.**

Metal complexes surround by ligand frameworks with various H-bond networks: [H<sub>3</sub>buea]<sup>3-</sup> (A), [RST]<sup>3-</sup> (B), and [H<sub>2</sub>2<sup>tol</sup>]<sup>3-</sup> (C). H-bonds donating groups are shown in blue, while accepting moieties are highlighted in red. The H-bond interactions are illustrated with black dotted lines.

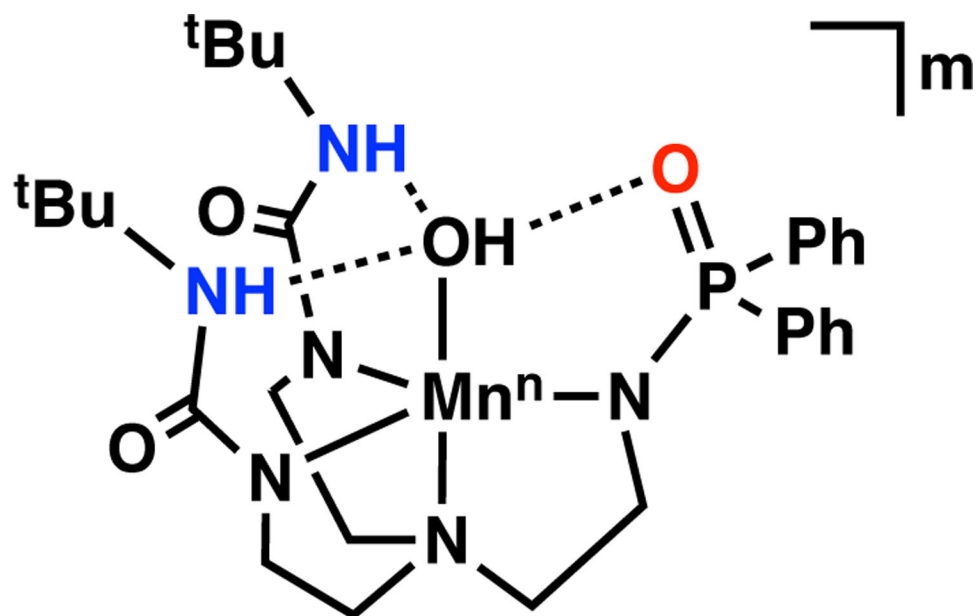


**Figure 2.** Metal complex within the [H<sub>2</sub>pout]<sup>3-</sup> framework where n = 2+, m = 2-; n = 3+, m = 1-; n = 4+, m = 0

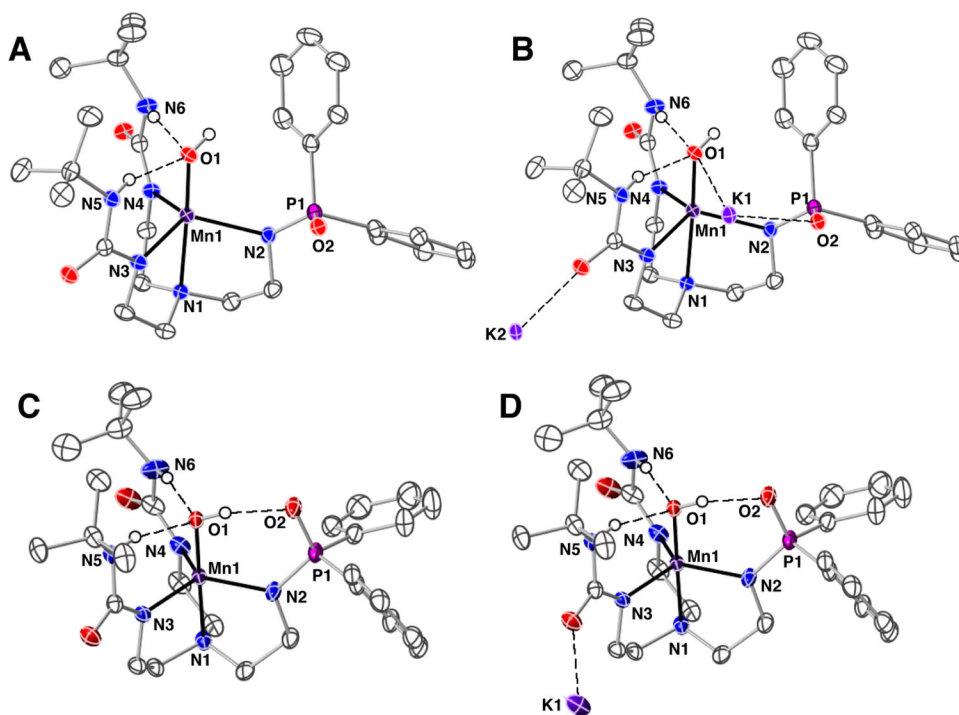


**Figure 3.** Thermal ellipsoid plots of  $[\text{Mn}^{\text{II}}\text{H}_2\text{pout}(\text{OH})]^{2-}$  (A),  $\text{K}_2[\text{Mn}^{\text{II}}\text{H}_2\text{pout}(\text{OH})]$  (B),  $[\text{Mn}^{\text{III}}\text{H}_2\text{pout}(\text{OH})]^-$  (C),  $\text{K}[\text{Mn}^{\text{III}}\text{H}_2\text{pout}(\text{OH})]$  (D). Thermal ellipsoids are drawn at the 50% probability level, only urea and hydroxido hydrogen atoms are shown for clarity.

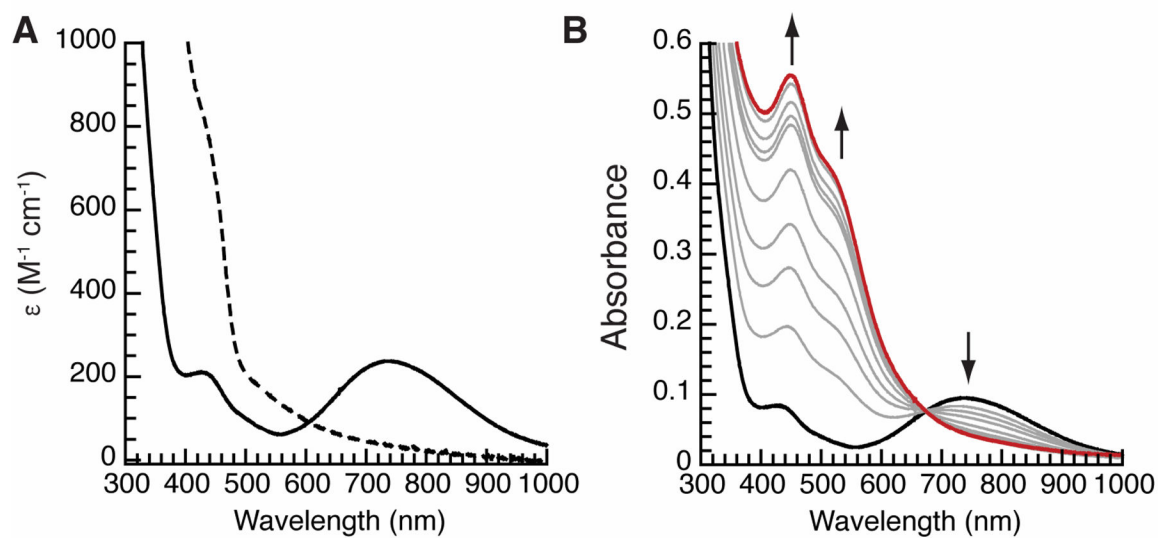


**Figure 4.** UV-visible spectra monitoring the conversion of  $[\text{Mn}^{\text{II}}\text{H}_2\text{pout}(\text{OH})]^{2-}$  (---) to  $[\text{Mn}^{\text{III}}\text{H}_2\text{pout}(\text{OH})]^-$  (—) (A) and  $[\text{Mn}^{\text{III}}\text{H}_2\text{pout}(\text{OH})]^-$  to  $[\text{Mn}^{\text{IV}}\text{H}_2\text{pout}(\text{OH})]$  (—) (B). Spectra were recorded in a 1:1 DMF:THF mixture at  $-80^\circ\text{C}$ .

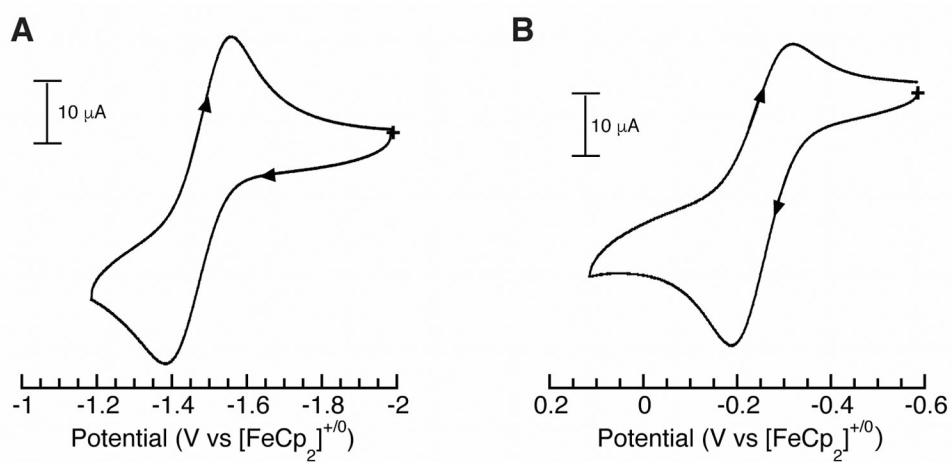


**Figure 5.** Cyclic voltammograms of  $[\text{Mn}^{\text{II}}\text{H}_2\text{pout}(\text{OH})]$  recorded in DMF:  $\text{Mn}^{\text{III/II}}$  couple (A),  $\text{Mn}^{\text{IV/III}}$  couple (B). Measurements were done at room temperature under Ar with a scan rate of  $100 \text{ mV s}^{-1}$ .

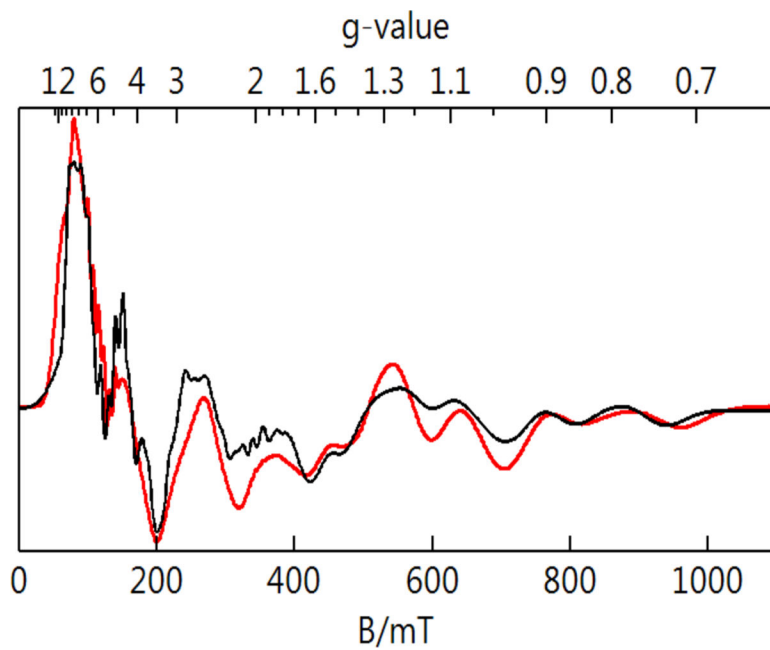


**Figure 6.** Perpendicular-mode EPR spectrum of a frozen solution of  $[\text{Mn}^{\text{II}}\text{H}_2\text{pout}(\text{OH})]^{2-}$  in 1:1 DMF:THF. Sample temperature 16 K, microwaves, 9.645 GHz, 0.2 mW. The black trace is a simulation for a  $S = 5/2$  species.

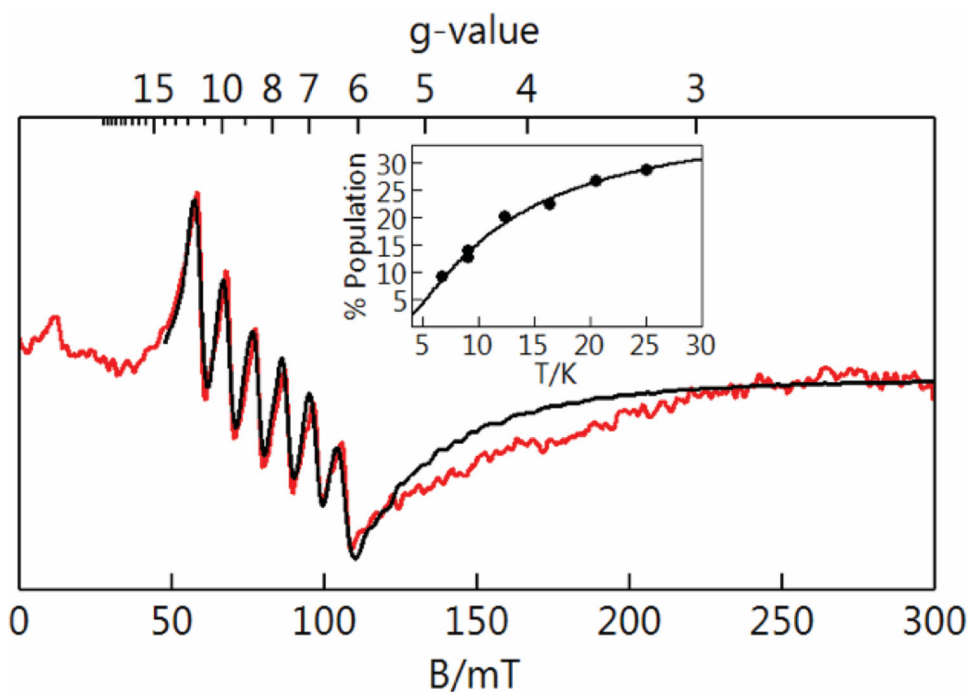


**Figure 7.** Parallel-mode EPR spectrum of a frozen solution of  $[\text{Mn}^{\text{III}}\text{H}_2\text{pout}(\text{OH})]^-$  in solvent 1:1 DMF:THF. Sample temperature 19 K, microwaves 9.318 GHz, 2 mW. The black trace is a simulation for a  $S = 2$  species. Inset: experimental signal intensity times temperature versus temperature (points) and the calculated % population of the EPR active doublet of  $S = 2$  and  $D = +2.7 \text{ cm}^{-1}$ .



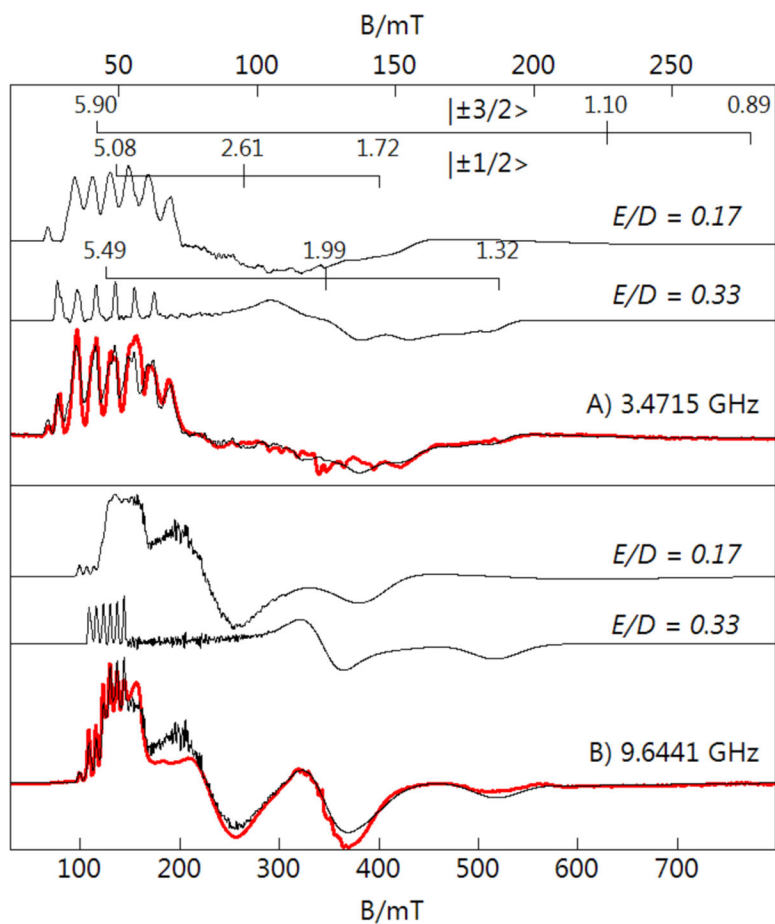


**Figure 8.** Perpendicular-mode EPR spectra of a 1:1 DMF:THF frozen solution  $[\text{Mn}^{\text{IV}}\text{H}_2\text{pout}(\text{OH})]$  at S-band (A) and X-band (B). Sample temperature was 5 K, microwave power was 0.03 mW for S-band and 0.2 mW for X-band. The black traces overlaid on the experimental spectra are the sum of the  $S = 3/2$  simulations for the  $E/D = 0.17$  and 0.33 species in a ratio of 70:30, respectively.

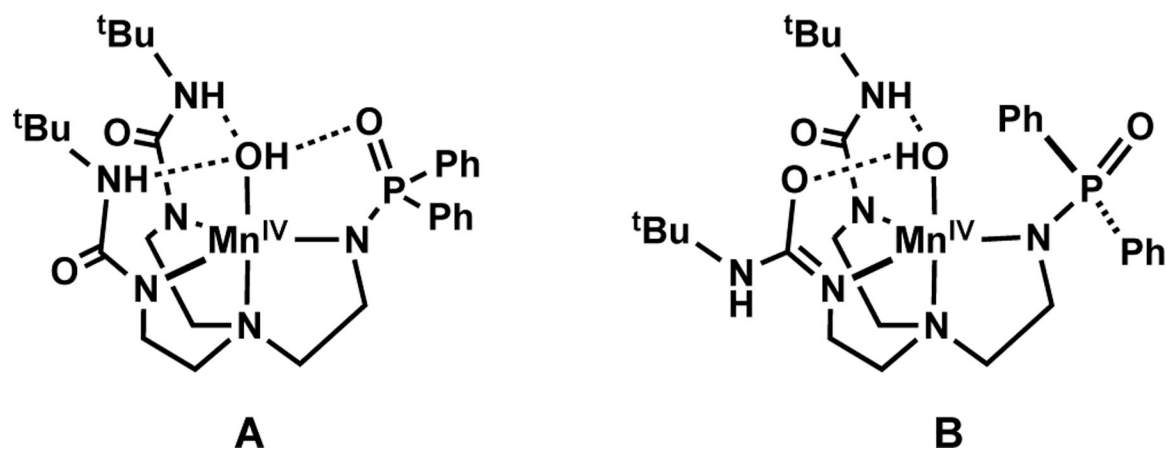
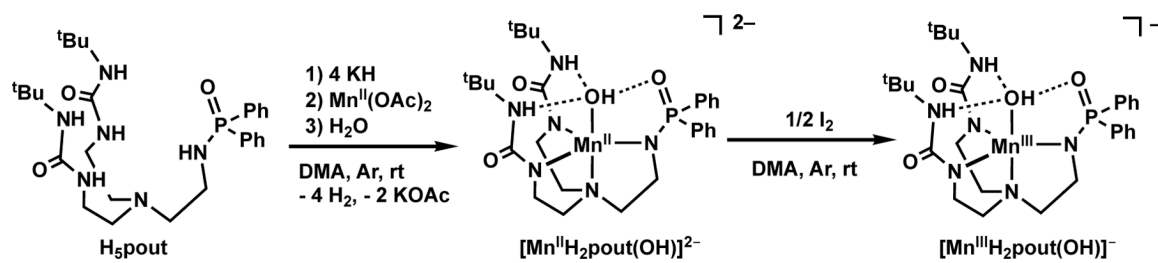
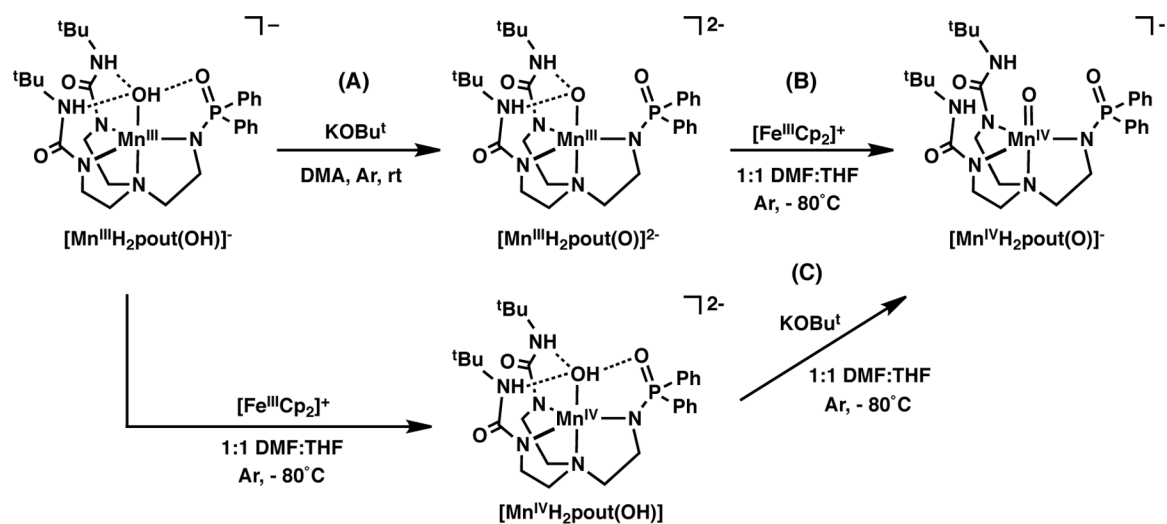


**Figure 9.**  
Possible structures for the two Mn<sup>IV</sup>-OH complexes of [Mn<sup>IV</sup>H<sub>2</sub>pout(OH)] determined from DFT.



**Scheme 1.**  
Preparation of Mn–OH complexes.



**Scheme 2.**  
Preparation of Mn-oxido complexes of [H<sub>2</sub>pout]<sup>3-</sup>.

**Table 1.**

Selected Bond Distances and Angles for  $K_2[Mn^{II}H_2pout(OH)]$  and  $K[Mn^{III}H_2pout(OH)]$  Determined by XRD and DFT Methods.

Bond Distances (Å) or Angles (°)	XRD	DFT	XRD	DFT
	$K_2[Mn^{II}H_2pout(OH)]$		$K[Mn^{III}H_2pout(OH)]$	
Mn(1)-O(1)	2.051(1)	2.07	1.834(1)	1.85
Mn(1)-N(1)	2.315(1)	2.46	2.054(2)	2.11
Mn(1)-N(2)	2.214(1)	2.17	2.056(2)	2.03
Mn(1)-N(3)	2.220(1)	2.15	2.035(2)	2.06
Mn(1)-N(4)	2.121(1)	2.20	2.068(2)	2.10
O(1)···O(2)	3.958(2)		2.685(2)	2.71
O(1)···N(5)	2.768(2)	2.79	2.776(2)	2.78
O(1)···N(6)	3.053(2)	2.83	2.773(2)	2.77
O(1)-Mn(1)-N(1)	170.13(5)	172	179.18(7)	178
O(1)-Mn(1)-N(2)	103.60(5)	100	97.36(6)	99
O(1)-Mn(1)-N(3)	93.48(5)	98	97.49(6)	98
O(1)-Mn(1)-N(4)	108.76(5)	111	98.82(6)	97
N(1)-Mn(1)-N(4)	78.68(5)	77	81.91(7)	82
N(1)-Mn(1)-N(2)	78.62(5)	77	81.96(6)	83
N(2)-Mn(1)-N(4)	112.73(5)	107	116.27(7)	118
N(3)-Mn(1)-N(1)	77.22(5)	77	82.53(6)	81
N(3)-Mn(1)-N(2)	119.46(5)	116	124.58(7)	125
N(3)-Mn(1)-N(4)	115.48(5)	122	113.59(7)	111

**Table 2.**EPR parameters of the  $[\text{Mn}^n\text{H}_2\text{pout}(\text{OH})]^m$  complexes

$[\text{Mn}^n\text{H}_2\text{pout}(\text{OH})]^m$	$S$	$D^a$	$E/D$	$g$	$ A ^b$
$\text{Mn}^{\text{II}}$	5/2	-0.24	0.065	2.00, 2.00, 2.00	$A_{\text{iso}} = 250$
$\text{Mn}^{\text{III}}$	2	+2.7	0.04	-, -, 2.01	$A_z = 270$
$\text{Mn}^{\text{IV}}(1)$	3/2	+0.8	0.33	2.00, 2.01, 1.98	152, 198, 183
$\text{Mn}^{\text{IV}}(2)$	3/2	+0.7	0.17	2.06, 1.96, 2.02	224, 188, 201

<sup>a</sup>cm<sup>-1</sup>; <sup>b</sup>MHz

**Table 3.**DFT Computed Metrical Parameters for Proposed Structures of [Mn<sup>IV</sup>H<sub>2</sub>pout(OH)].

<b>Bond Distances (Å) or Angles (°)</b>	<b>A<sup>a</sup></b>	<b>B<sup>a</sup></b>
Mn(1)-O(1)	1.80	1.78
Mn(1)-N(1)	2.15	2.11
Mn(1)-N(2)	1.91	1.92
Mn(1)-N(3)	1.93	2.01
Mn(1)-N(4)	1.96	1.91
O(1)···O(2)	2.58	2.59
O(1)···N(5)	2.73	4.36
O(1)···N(6)	2.76	2.70
O(1)-Mn(1)-N(1)	177	177
O(1)-Mn(1)-N(2)	97	97
O(1)-Mn(1)-N(3)	98	95
O(1)-Mn(1)-N(4)	96	98
N(1)-Mn(1)-N(4)	82	84
N(1)-Mn(1)-N(2)	83	84
N(2)-Mn(1)-N(4)	132	114
N(3)-Mn(1)-N(1)	84	82
N(3)-Mn(1)-N(2)	110	130
N(3)-Mn(1)-N(4)	114	112

<sup>a</sup> see Figure 9